PAPER

Check for updates

Defect engineering of two-dimensional Nb-based oxynitrides for visible-light-driven water splitting to produce H2 and O2†

Chang Xu,[a] Yan Wang,[*a] Quansheng Guo[b] and Xin Wang [ID] [*a]

Two-dimensional (2D) Nb-based oxynitrides are promising visible-light-responsive photocatalysts for the water splitting reaction, but their photocatalytic activity is degraded by the formation of reduced Nb^{5+} species and O^{2-} vacancies. To understand the influence of nitridation on the formation of crystal defects, this study synthesized a series of Nb-based oxynitrides through the nitridation of $LaKNaNb_{1-x}Ta_xO_5$ (x = 0, 0.2, 0.4, 0.6, 0.8, 1.0). During nitridation, K and Na species volatilized, which helped transform the exterior of $LaKNaNb_{1-x}Ta_xO_5$ into a lattice-matched oxynitride shell. Ta inhibited defect formation, yielding Nb-based oxynitrides with a tunable bandgap between 1.77 and 2.12 eV, straddling the H2 and O2 evolution potentials. After loading with Rh and CoO_x cocatalysts, these oxynitrides exhibited good photocatalytic activity for H2 and O2 evolution in visible light (650–750 nm). The nitrided $LaKNaTaO_5$ and $LaKNaNb_{0.8}Ta_{0.2}O_5$ delivered the maximum H2 (19.37 µmol h^{-1}) and O2 (22.81 µmol h^{-1}) evolution rates, respectively. This work provides a strategy for preparing oxynitrides with low defect densities and demonstrates the promising performance of Nb-based oxynitrides for water splitting.

Introduction

Photocatalytic water splitting into hydrogen (H2) and oxygen (O2) is regarded as one of the most promising strategies for solving the global energy crisis and mitigating environmental problems.[1–3] In the solar spectrum, UV light accounts for less than 5% of the energy in sunlight, whereas visible light constitutes approximately 54%.[4–6] In order to achieve high photocatalytic efficiency, semiconductors with narrow band gap energies (E_g) that are capable of absorbing the wide wavelengths of visible light are very attractive.[7,8] Recently, metal oxynitrides are being reported continuously, whose E_g is significantly narrower than that of conventional metal oxides because N 2p orbitals provide a new valence band (VB) that is more negative than that provided by O 2p orbitals.[9–11]

Among these oxynitrides, Nb-based oxynitrides exhibit a broad light absorption band in the visible light region, with λ_{max} values up to approximately 750 nm, which is much higher than their Ta-based counterparts.[12–15] To date, various Nb-based oxynitrides, such as $CaNbO_2N$ (λ_{max} = 600 nm), $SrNbO_2N$ (λ_{max} = 690 nm), $BaNbO_2N$ (λ_{max} = 740 nm) and $LaNbON_2$ (λ_{max} = 750 nm) have been synthesized by nitriding oxide precursors under

an NH3 flow and applied for photocatalysis. For instance, $CaNbO_2N$ was found to be active for O2 evolution from a $AgNO_3$ aqueous solution.[12] The optimal nitridation temperature in that study was determined to be 1023 K. $SrNbO_2N$ prepared by nitriding $Sr_2Nb_2O_7$ or $SrNbO_3$ exhibited enhanced activity for photoelectrochemical water splitting, with a current density of 0.77 mA cm^{-2} at 1.2 V *versus* the reversible hydrogen electrode (RHE).[13] Meanwhile, Hisatomi *et al.* improved the crystallinity and uniformity of $BaNbO_2N$ by adding $BaCO_3$ into the $Ba_5Nb_4O_{15}$ precursor during the synthesis procedure, and the resulting $BaNbO_2N$ exhibited enhanced O2 evolution activity by utilizing photons with wavelengths of up to 740 nm.[14] Recently, Wang *et al.* prepared $LaNbON_2$ with exposed metastable {010} facets by nitriding a plate-like $LaKNaNbO_5$ precursor. In combination with a CoO_x co-catalyst, $LaNbON_2$ exhibited enhanced photocatalytic activity for O2 evolution, with an apparent quantum yield of 0.82%, whereas conventional $LaNbON_2$ was almost inactive.[15] However, nitridation is a harsh process. N doping always causes a charge imbalance as a result of aliovalent O^{2-}/N^{3-} exchange, yielding numerous crystal defects that are detrimental to the photocatalytic performance of oxynitrides.[16,17] Like Nb-based oxynitrides, it still exhibits negligible photocatalytic activity, especially for photocatalyzing H2 evolution, because of the formation of large amounts of reduced Nb^{5+} species and O^{2-} vacancies during the nitridation process. These vacancies can act as recombination and trapping centers for photoexcited charges, resulting in a decrease in charge separation efficiency.[18–20] Moreover, a low concentration

aShenzhen Institute of Advanced Technology, Chinese Academy of Sciences, Shenzhen 518055, China. E-mail: xin.wang2@siat.ac.cn

bSchool of Materials Science and Engineering, Hubei University, Wuhan 430062, China
† Electronic supplementary information (ESI) available. See DOI: https://doi.org/10.1039/d2na00915c

of the N dopant inevitably can also decrease the absorption coefficient of N-doped oxides in the visible light region.[21] Therefore, undoped oxynitrides containing a stoichiometric amount of N in their crystal structure are highly desirable, which can guarantee strong visible light absorption through band-to-band electron transitions and the development of Nb-based oxynitrides with low defect densities remains a challenge.

Herein, we synthesized a series of Nb-based oxynitrides through the nitridation of $LaKNaNb_{1-x}Ta_xO_5$ ($x = 0, 0.2, 0.4, 0.6, 0.8, 1.0$). By introducing Ta, the formation of defects in their crystal structure is effectively inhibited yielding a tunable bandgap. In the meantime, volatilization of K and Na species during nitridation promoted $LaKNaNb_{1-x}Ta_xO_5$ crystal surfaces to be transformed into lattice-matching oxynitrides, forming a core–shell structure. Considering the above mentioned enhanced properties, these oxynitrides exhibited good photocatalytic activity for H_2 and O_2 evolution in visible light (650–750 nm).

Results and discussion

Fig. 1 illustrates the crystal structure of $LaKNaNb_{1-x}Ta_xO_5$, which is similar to that of $LaKNaNbO_5$ (Fig. S1†) and has $LaNaNbO_5^-$ layers along the [001] direction with K^+ ions occupying the spaces between the layers. Each $LaNaNbO_5$ layer is arranged in a "checkerboard" pattern, where NaO_5 and NbO_5 square pyramids are arranged in alternating rows.[23,24] In $LaKNaNb_{1-x}Ta_xO_5$, a fraction of the Nb atoms are substituted with Ta atoms. Accordingly, $LaNbON_2$ has an orthorhombic perovskite structure with the space group $Pnma$ (Fig. 1). The unit cell parameters of $LaNbON_2$ are $a = 5.7221$ Å, $b = 8.0684$ Å, and $c = 5.7428$ Å.[25] As the amount of Ta^{5+} increases, $Nb_xTa_{1-x}O_5$ square pyramids in $LaNb_{1-x}Ta_xON_2$ become distorted because Ta–(O, N) bonds (2.056 Å) are shorter than Nb–(O, N) bonds (2.064 Å). As a result, pure $LaTaON_2$ demonstrated a monoclinic perovskite structure, indicating the successful substitution of Nb by Ta in the oxynitride lattice with angles from 90° to 135° between the a- and c-axes (Fig. S2†).

Plate-like $LaKNaNb_{1-x}Ta_xO_5$ was prepared by a NaOH/KOH flux method as previously reported.[26,27] Specifically, 5 mmol of La_2O_3 and 5 mmol in total of Ta_2O_5 and Nb_2O_5 at various molar ratios (0 : 5, 1 : 4, 2 : 3, 3 : 2, 4 : 1, and 5 : 0) were combined and finely ground in a mortar, after which the mixture was
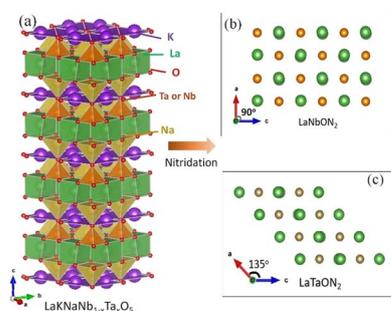
transferred to an alumina crucible containing an excess of KOH (10 g) and NaOH (5 g). Subsequently, the mixture was calcined at 873 K for 3 h and aged at 773 K for 15 h. In this synthesis, KOH and NaOH were in excess during synthesis to serve as major flux components for the crystal growth of $LaKNaNb_{1-x}Ta_xO_5$ oxides, resulting in large, highly crystalline products. A scheme of the synthetic procedure is shown in Fig. S3.†

The XRD patterns of the $LaKNaNb_{1-x}Ta_xO_5$ precursor ($x = 0, 0.2, 0.4, 0.6, 0.8,$ and 1) were nearly identical to those of the tetragonal $LaKNaNbO_5$ phase with a space group of $P4/nmm$, indicating the phase purity of the flux-grown oxide crystals (Fig. 2a). Notably, the intensity of the diffraction peak at 10° for $LaKNaNbO_5$ was enhanced, indicating the exposure of the {001} facets on the surface. Interestingly, with the increasing Ta content, the position of the diffraction peak of $LaKNaNb_{1-x}Ta_xO_5$ shifted to a slightly higher angle than that of the $LaKNaNbO_5$ crystals, indicating that the substitution of Nb with Ta caused a decrease in the crystal size and an overall contraction of the lattice parameters in the $LaKNaNb_{1-x}Ta_xO_5$ samples.[28,29] After nitridation at 1173 K for 4 h, peaks attributable to the $LaNbON_2$ phase were observed together with intense $LaKNaNbO_5$ peaks, which could be ascribed to the transformation of the surface of the $LaKNaNbO_5$ precursor into $LaNbON_2$ during nitridation, while the crystal interior remained an oxide (Fig. 2b). Interestingly, the intensity of the diffraction peaks attributed to the $LaNb_{1-x}Ta_xON_2$ phase became weaker with the increasing Ta content. This finding indicates that introducing Ta species can slow down the transformation from the $LaKNaNb_{1-x}Ta_xO_5$ precursor into its lattice-matched $LaNb_{1-x}Ta_xON_2$ owing to the lower electronegativity of the Ta

Fig. 1 (a) Crystal structure of layered $LaKNaNb_{1-x}Ta_xO_5$. (b and c) Views of the (010) facets of (b) $LaNbON_2$, and (c) $LaTaON_2$. The crystal structures were visualized using the VESTA suite of programs.[22]
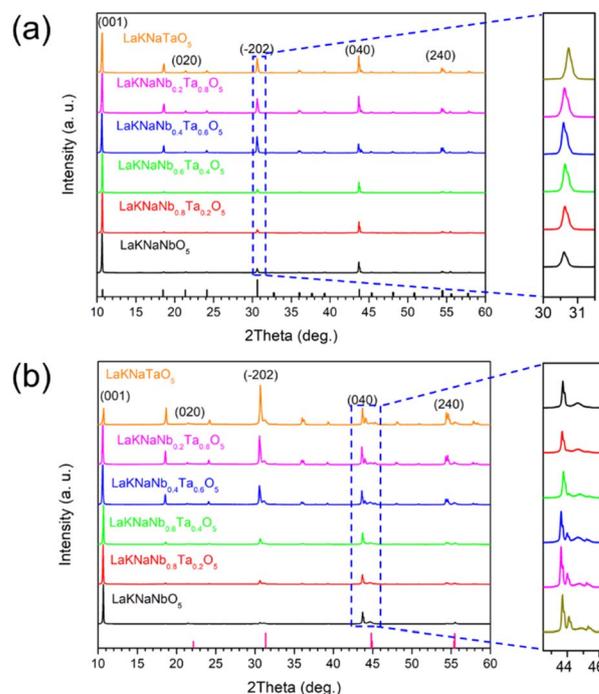

Fig. 2 XRD patterns of the (a) layered $LaKNaNb_{1-x}Ta_xO_5$ oxide precursors and (b) nitrided $LaKNaNb_{1-x}Ta_xO_5$ ($x = 0, 0.2, 0.4, 0.6, 0.8, 1.0$).

species. Consequently, this transformation process can be finely tuned by varying the degree of substitution.

SEM was used to investigate the size and morphology of the resulting products. As shown in Fig. 3a and b, the oxide precursors that were not thermally aged at 773 K for 15 h exhibited an incomplete plate morphology with a rough surface. In contrast, the aged LaKNaNb$_{1-x}$Ta$_x$O$_5$ showed a plate-like shape with a smooth surface, indicating that the long-term flux process facilitates the synthesis of oxide precursors with controllable morphology and high crystallinity (Fig. S4†). After nitridation, the prepared sample maintained its plate-like shape but became porous, as illustrated in Fig. 3c and S5.† The corresponding cross-sectional SEM image in Fig. 3d shows the formation of a core–shell structure based on a porous oxynitride shell on a dense oxide core. The core–shell structure has the advantage of generating as many oxynitrides on the oxide surface as possible during the mild nitridation process while minimizing the number of crystal defects of oxynitrides as much as possible.[30]

The exposed facets of oxynitrides after nitridation were confirmed using TEM and high-resolution TEM (HRTEM) images (Fig. 4a and b, respectively), where the interplanar distances associated with the (200) and (002) facets of LaNb$_{1-x}$Ta$_x$ON$_2$ were 0.228 and 0.202 nm, respectively, with an angle of approximately 105°. This finding indicates that the La and Nb atoms are located in the expected positions in the orthorhombic structure viewed in the [010] direction, which energetically favors the {010} facet on the surface. The energy dispersive spectroscopy (EDS) mapping images shown in Fig. 4c show that the resulting product is composed of La, K, Na, Nb, Ta, O, and N. Comparing the atomic ratios obtained from the EDS spectrum after nitridation with the known composition before nitridation reveals that the amounts of K and Na decreased dramatically during the nitridation process (Fig. S6†).
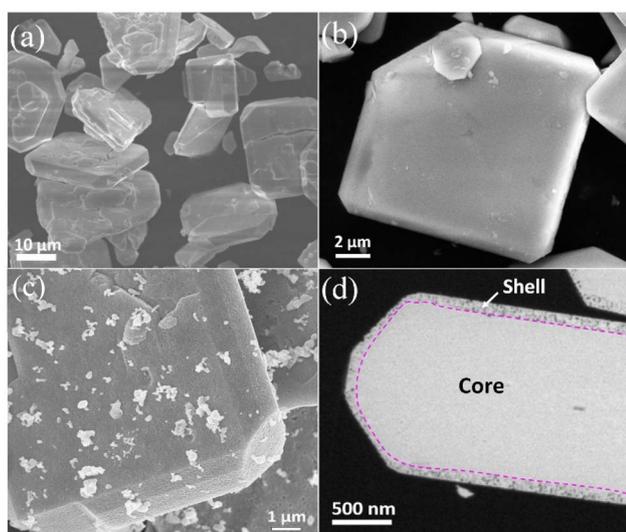

Fig. 4 (a) TEM and (b) HRTEM images and (c) EDS elemental maps of plate-like LaKNaNb$_{0.8}$Ta$_{0.2}$O$_5$ nitrided at 1123 K for 4 h. The atomic ratios were approximately La/Nb ≈ 1.3, K/Nb < 0.05, Na/Nb < 0.05, O/Nb ≈ 1.3, and N/Nb ≈ 2.5.

In the photographs of the nitrided LaKNaNb$_{1-x}$Ta$_x$O$_5$ powder samples (Fig. 5a), the color of the samples clearly changes from dark brown to orange with the increasing amount of Ta^{5+}. Meanwhile, in the UV-vis diffraction reflectance spectra (DRS) of the nitrided LaKNaNb$_{1-x}$Ta$_x$O$_5$ samples presented in Fig. 5b, the absorption edges of the nitrided LaKNaNb$_{1-x}$Ta$_x$O$_5$ samples gradually blue-shifted from 720 to 600 nm with the increasing Ta content, indicating that the bandgap energies of these materials were greater than those of pure LaNbON$_2$ ($\lambda \approx$ 740 nm) during mild nitridation.[15] The corresponding Tauc plots of the nitrided LaKNaNb$_{1-x}$Ta$_x$O$_5$ samples (Fig. 5c) based on the UV-vis DRS spectra reveal that the bandgap energy increased monotonically from 1.77 to 2.12 eV with increasing substitution with Ta^{5+}. Moreover, their bandgap positions were estimated based on the VB XPS data (Fig. S7 and Table S1†)

Fig. 3 SEM images of layered LaKNaNb$_{1-x}$Ta$_x$O$_5$ (a) calcined at 873 K for 3 h and (b) then aged at 773 K for 15 h (c) surface and (d) cross-sectional SEM images of LaKNaNb$_{1-x}$Ta$_x$O$_5$ powder nitrided at 1123 K for 4 h, revealing the porous surface.

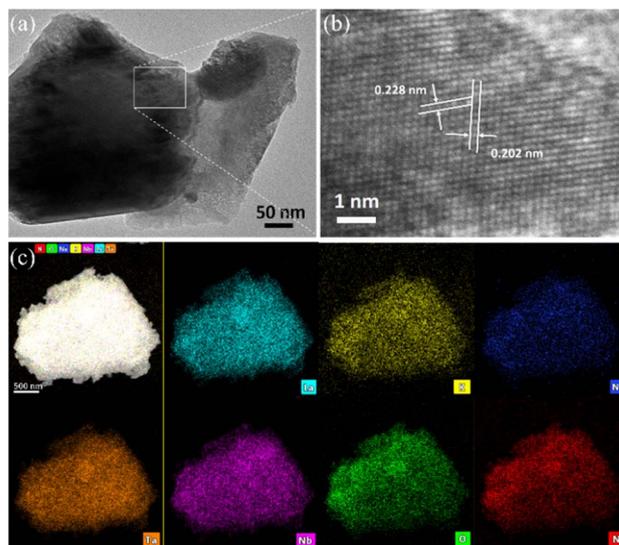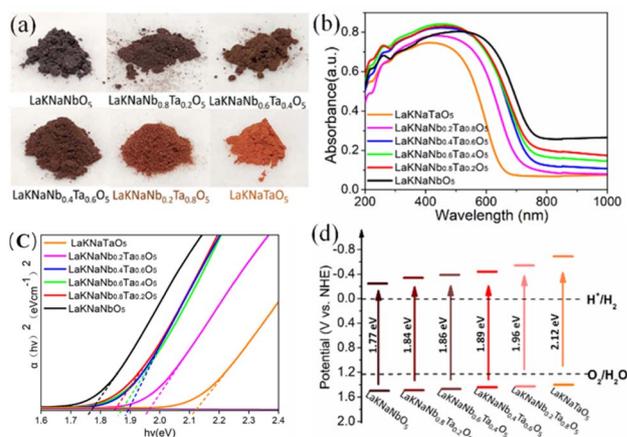Fig. 5 (a) Photographs, (b) UV-vis DRS, (c) corresponding Tauc plots, and (d) band structure diagrams of the LaKNaNb$_{1-x}$Ta$_x$O$_5$ samples (x = 0, 0.2, 0.4, 0.6, 0.8, 1.0) nitrided at 1123 K for 4 h.

along with the Tauc plots. As shown in Fig. 5d, the VB of the nitrided LaKNaNb$_{1-x}$Ta$_x$O$_5$ samples remained almost unchanged with the increasing amount of Ta^{5+}, and the enlarged bandgaps of these samples mainly resulted from the upshift of the conduction band (CB), demonstrating that the Ta CB orbitals mainly contributed to the Ta 5d orbitals.

Notably, the nitrided LaKNaNbO$_5$ samples exhibited obvious background absorption at wavelengths >650 nm, which could be ascribed to the formation of a large amount of reduced Nb^{5+} species as well as O^{2-} vacancies.[18,19] Reduced metallic species are known not to exhibit photocatalytic activity owing to bandgap excitation, and such defect states usually generated by prolonged exposure to NH$_3$ during nitridation at high temperatures can act as recombination and trapping centers for photoexcited charges. In particular, the background absorption became much weaker as the amount of Ta^{5+} increased, indicating that fewer crystal defects formed during the nitridation process. This is because Ta is less electronegative than Nb, which slowed down the nitridation process, thus inhibiting the typical formation of crystal defects in the nitrided LaKNaNb$_{1-x}$Ta$_x$O$_5$ samples.

The chemical compositions of the nitrided LaKNaNb$_{1-x}$Ta$_x$O$_5$ samples were analyzed using high-resolution XPS. The survey spectra are shown in Fig. S8a.† They confirm the presence of Ta, Nb, N and O in the as-prepared nitrided LaKNaNb$_{1-x}$Ta$_x$O$_5$ samples. By comparing with the unnitrided sample (Fig. S8b†), the presence of N on the surface of nitrided LaKNaNb$_{1-x}$Ta$_x$O$_5$ can be confirmed. As shown in Fig. 6a, the

Nb valence species at the surface of the nitrided LaKNaNb$_{1-x}$Ta$_x$O$_5$ sample were evaluated to investigate the effect of adding Ta^{5+} on the reduction of Nb^{5+} during nitridation. The Nb 3d XPS spectra were deconvoluted into peaks for three different Nb valence species,[31] Nb^{5+}, Nb^{4+}, and Nb^{3+}, based on the tailing of the peaks toward lower binding energies, demonstrating that more than one chemical state exists in the samples. Here, the presence of Nb^{4+} and Nb^{3+} indicates the reduction of the Nb^{5+} species derived from NH$_3$ nitridation. These reduced Nb^{4+} and Nb^{3+} species can act as charge trapping and recombination centers for the photoexcited electrons and holes. Table S2† summarizes the proportions of surface Nb species in the nitrided LaKNaNb$_{1-x}$Ta$_x$O$_5$ sample with different amounts of Ta^{5+}. With increasing Ta^{5+}, the nitrided LaKNaNb$_{1-x}$Ta$_x$O$_5$ samples exhibited the decreased presence of reduced Nb species (both Nb^{3+} and Nb^{4+}) from 82.06% for nitrided LaKNaNbO$_5$ without Ta to 48.61% for nitrided LaKNaNb$_{0.2}$Ta$_{0.8}$O$_5$. These results indicate that substitution with Ta^{5+} species can effectively inhibit the reduction of Nb.

A similar phenomenon was also observed for the Ta^{5+} species in the deconvoluted Ta 4f XPS spectra of the nitrided LaKNaNb$_{1-x}$Ta$_x$O$_5$ samples, which can be deconvoluted into two different reduced Ta species,[32,33] Ta^{5+} and Ta^{4+}, based on the binding energies (Fig. 6b).[30] The increasing Ta^{5+} content was found to inhibit the reduction of Ta^{5+} species, from 70.72% for the nitrided LaKNaTa$_{0.2}$Nb$_{0.8}$O$_5$ sample to 25.84% for the nitrided LaKNaTaO$_5$ sample (Table S3†). Therefore, according to the band diagrams and XPS data, the replacement of Nb^{5+} with Ta^{5+} evidently hindered the reduction of both Nb and Ta during nitridation, thus tuning the band structure of the nitrided LaKNaNb$_{1-x}$Ta$_x$O$_5$ sample while maintaining the visible-light-driven photocatalytic activity.

Moreover, the O 1s state of the oxide precursor could be decomposed into two overlapping peaks centered at 529.6 and 532.5 eV (Fig. S9†). These two peaks could be attributed to lattice oxygen in the oxide (O$_L$) and hydroxyl groups (O–H) that adsorbed on the sample surfaces during sample handling, respectively.[34,35] As illustrated in Fig. S10,† a new peak centered at 531.4 eV appeared after nitridation, the intensity of which is partly related to the concentration of O^{2-} vacancies. Notably, the intensity of the O$_v$ peak decreased from 43.27% for LaKNaNbO$_5$ (no Ta^{5+}) to 20.75% for LaKNaTaO$_5$ in which Nb^{5+} was completely replaced with Ta^{5+}, indicating that fewer O^{2-} vacancies formed in the nitrided samples (Table S4†).

The photocatalytic performance of the nitrided LaKNaNb$_{1-x}$Ta$_x$O$_5$ samples toward the evolution of H$_2$ and O$_2$ under visible light was examined in an aqueous methanol solution loaded with a Rh co-catalyst and an aqueous AgNO$_3$ solution loaded with the CoO$_x$ co-catalyst. Fig. 7a shows the H$_2$ evolution as a function of time. Evidently, all the nitrided LaKNaNb$_{1-x}$Ta$_x$O$_5$ samples showed photocatalytic activity for H$_2$ evolution. However, the nitrided sample without Ta^{5+} showed the lowest activity (0.2635 μmol h^{-1}, Table S5†), which could be ascribed to the formation of large amounts of reduced Nb^{5+} species and O^{2-} vacancies in the LaNbON$_2$ shells, as discussed in the analyses of the DRS and XPS data (Fig. 5b and 6). In contrast, the activity of the nitrided LaKNaNbO$_5$ sample was

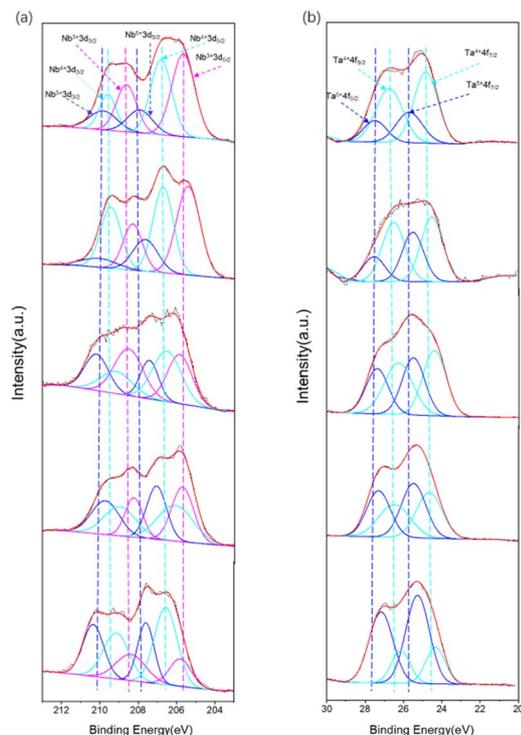**Fig. 6** High-resolution XPS spectra of the LaKNaNb$_{1-x}$Ta$_x$O$_5$ samples nitrided at 1123 K for 4 h: (a) Nb 3d spectra for x = 0, 0.2, 0.4, 0.6 and 0.8 from up to down; (b) Ta 4f spectra for x = 0.2, 0.4, 0.6, 0.8 and 1.0 (no Nb) from up to down.
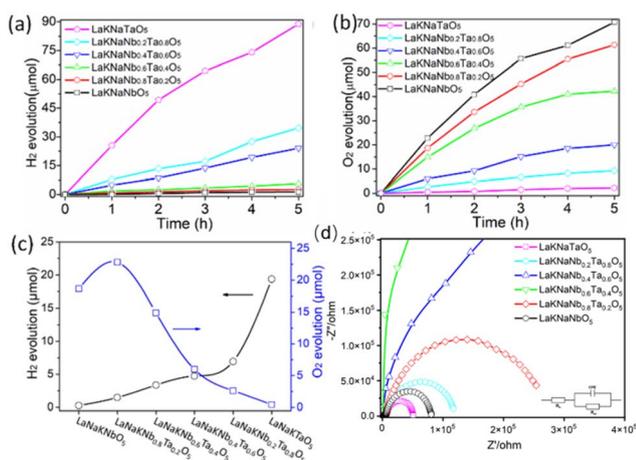
Fig. 7 Photocatalytic performance of LaKNaNb$_{1-x}$Ta$_x$O$_5$ nitrided at 1123 K for 4 h (x = 0, 0.2, 0.4, 0.6, 0.8, 1.0): (a) H$_2$ and (b) O$_2$ evolution as a function of time, (c) H$_2$ and O$_2$ evolution rates, and (d) EIS spectra recorded under visible light illumination. Reaction conditions for H$_2$ evolution: 150 mL of aqueous methanol (20 vol%), photocatalyst: 300 mg, co-catalyst: 0.5 wt% Rh, loading method: impregnation with H$_2$ reduction, light source: a 300 W xenon lamp ($\lambda \geq$ 420 nm), reaction cell: a top-irradiation cell with a Pyrex window. Reaction conditions for O$_2$ evolution: 150 mL of an aqueous 50 mM AgNO$_3$ solution containing 0.20 g of La$_2$O$_3$, photocatalyst: 300 mg, co-catalyst: 0.5 wt% CoO$_x$, light source: a 300 W xenon lamp ($\lambda \geq$ 420 nm), reaction cell: a top-irradiation cell with a Pyrex window.

enhanced by the increased substitution of Nb with Ta^{5+}. Thus, introducing Ta^{5+} species effectively inhibited the reduction of Nb species, thereby decreasing the possibility of photo-generated charges recombining at defects and enhancing the photocatalytic activity toward H$_2$ evolution.[15,18,30] After complete Ta^{5+} substitution, the nitrided LaKNaTaO$_5$ sample showed the highest photocatalytic H$_2$ evolution activity (19.37 μmol h^{-1}) because of the presence of a low-defect-density LaTaON$_2$ shell on the lattice-matched LaKNaTaO$_5$ core.

Moreover, the photocatalytic activity of nitrided LaKNaNb$_{1-x}$Ta$_x$O$_5$ for O$_2$ evolution was evaluated by modifying the CoO$_x$ co-catalyst (Fig. 7b). The treatment temperature of the CoO$_x$ co-catalyst modified on the sample surface was first optimized (Fig. S11†). A low treatment temperature resulted in low photocatalytic activity for O$_2$ evolution owing to weak interfacial bonding between the CoO$_x$ co-catalyst and LaNb$_{1-x}$Ta$_x$ON$_2$. On the other hand, a high treatment temperature above 873 K dramatically decreased the photocatalytic activity for O$_2$ evolution, which could be ascribed to the severe aggregation of the CoO$_x$ co-catalyst at high temperature. Therefore, the sample that was treated at ~773 K showed the highest photocatalytic activity for O$_2$ evolution owing to its well-integrated interface between the CoO$_x$ co-catalyst and LaNb$_{1-x}$Ta$_x$ON$_2$.[36] Although the nitrided LaKNaNbO$_5$ sample without Ta possessed a large number of crystal defects, it showed high photocatalytic activity for O$_2$ evolution (18.65 mol h^{-1}), which could be ascribed to the exposure of metastable {010} facets on the surface of LaNbON$_2$ crystals. These facets enabled photogenerated electrons to transfer from the interior of the oxynitride to its surface along the [010] direction, thus improving the charge separation efficiency.[15] The

photocatalytic O$_2$ evolution activity of nitrided LaKNaNb$_{0.8}$Ta$_{0.2}$O$_5$ (i.e., substituted with 20% Ta^{5+}) was the highest (22.81 μmol h^{-1}). However, higher Ta^{5+} contents decreased the photocatalytic O$_2$ evolution activity of the photocatalysts, even though their defect densities were lower in the formed oxynitride. This could be attributed to the fact that a greater Ta content decreased the transformation of LaKNaNb$_{1-x}$Ta$_x$O$_5$ into LaNb$_{1-x}$Ta$_x$ON$_2$. This phenomenon was confirmed using the XRD results shown in Fig. 2b.

Overall, the nitrided LaKNaNb$_{1-x}$Ta$_x$O$_5$ samples showed photocatalytic activity for both H$_2$ and O$_2$ evolution. This activity can also be finely tuned by varying the Ta^{5+} substitution content, which indicates that these oxynitrides have a bandgap straddling the H$_2$ and O$_2$ evolution potentials and thus show promise for use in the water splitting reactions (Fig. 7c). Furthermore, electrochemical impedance spectra (EIS) were recorded to further confirm the charge separation ability of these nitrided LaKNaNb$_{1-x}$Ta$_x$O$_5$ samples. As illustrated in Fig. 7d, nitrided LaKNaTaO$_5$ exhibited a smaller arc radius than nitrided LaKNaNbO$_5$, demonstrating a smaller resistance to charge transfer, which could be related to the lower amount of crystal defects in the former.[37,38] Interestingly, pure nitrided LaKNaNbO$_5$ and LaKNaTaO$_5$ both exhibited a lower resistance to charge transfer than the nitrided LaKNaNb$_{1-x}$Ta$_x$O$_5$ samples, suggesting that the Ta substitution distorted the lattice in the LaKNaNb$_{1-x}$Ta$_x$O$_5$ precursor. Moreover, regarding the stability performance of the nitrided LaKNaNb$_{1-x}$Ta$_x$O$_5$ samples, we carried out XPS analysis on nitrided LaKNaNb$_{0.8}$Ta$_{0.2}$O$_5$ before and after the photocatalytic H$_2$ production reaction, which shows no obvious difference between fresh and used catalysts (Fig. S12 and S13†). The detailed peak contents are provided in Table S6.† The ratio of N 1s/Nb 3d decreased slightly from 0.33 to 0.28, and the ratio of N 1s/Ta 4f decreased from 0.86 to 0.80. This result indicates a small decrease in the amount of N on the surface of the sample, which suggests that the nitrided LaKNaNb$_{1-x}$Ta$_x$O$_5$ samples remained stable in this photocatalytic system. These findings provide the basis for further studies on optimizing the nitridation temperature and heat treatment time of oxide precursors to improve the photocatalytic activity of oxynitrides for H$_2$ and O$_2$ evolution.

Conclusion

We investigated the nitridation of layered LaKNaNb$_{1-x}$Ta$_x$O$_5$ oxides and its effect on both crystal defects and the bandgap energy. During nitridation, the volatilization of K and Na species promoted the transformation of the surface of LaKNaNb$_{1-x}$Ta$_x$O$_5$ crystals into lattice-matched oxynitrides, thus forming a core–shell structure. Moreover, introducing Ta species decreased the defect densities, yielding Nb-based oxynitrides with a tunable bandgap from 1.77 to 2.12 eV, which straddled the H$_2$ and O$_2$ evolution potentials. As a result, these oxynitrides exhibited good photocatalytic activities for H$_2$ (19.37 μmol h^{-1}) and O$_2$ (22.81 μmol h^{-1}) evolution, which utilized visible light wavelengths between 650 and 750 nm. This work provides a novel strategy for preparing oxynitrides with a tunable bandgap and low defect densities, thus uncovering

the prospects of Nb-based oxynitrides for the overall water splitting reaction.

Experimental section

Materials

La_2O_3, Ta_2O_5, and Nb_2O_5 precursors and NaOH and KOH fluxing agents were all obtained from Macklin. $Co(NO_3)_2 \cdot 6H_2O$ and $RhCl_3 \cdot 3H_2O$ co-catalyst precursors were purchased from Sigma-Aldrich.

Synthesis of LaKNaNb$_{1-x}$Ta$_x$O$_5$. 2D layered LaKNaNb$_{1-x}$-Ta$_x$O$_5$ oxide precursors were synthesized using the NaOH/KOH flux method, as reported previously.[26,27] In this synthesis, Ta_2O_5 and Nb_2O_5 (5 mmol in total) at a certain molar ratio (0:5, 1:4, 2:3, 3:2, 4:1, and 5:0) were mixed with La_2O_3 (5 mmol) and finely ground in a mortar. Subsequently, the mixture was added to an alumina crucible containing excess KOH (10 g) and NaOH (5 g). The crucible was then placed in a furnace heated to 873 K at a rate of 10 K min^{-1}. This temperature was maintained for 3 h and then held at 773 K for 15 h. The furnace was subsequently allowed to cool naturally to room temperature. Afterward, the product was washed with ultrapure water at 343 K for 2 h and centrifuged twice to remove any residual KOH and NaOH. The powdered product was completely dried by heating at 313 K under vacuum overnight.

Synthesis of Nb-based oxynitrides. The as-prepared LaKNaNb$_{1-x}$Ta$_x$O$_5$ was subjected to a mild nitridation process in a tube furnace under an NH_3 atmosphere. For each sample, 0.4 g of LaKNaNb$_{1-x}$Ta$_x$O$_5$ was transferred into an alumina tube and then nitrided at various temperatures ranging from 1123 K for 4 h under a flow of gaseous NH_3 at 200 mL min^{-1}. The powder was then collected for further use.

Deposition of Co-catalysts. To load the photocatalyst with the Rh co-catalyst, 0.3 g of the powder was dispersed in a specific volume of an aqueous $RhCl_3 \cdot 3H_2O$ solution. The solution was completely evaporated by heating in a water bath at 353 K under stirring, after which the powder was collected and reduced at 473 K for 1 h under a flow of 5% H_2/N_2 (200 mL min^{-1}). To load the photocatalyst with the CoO_x co-catalyst, 0.3 g of the powder was added to 1.5 mL of an aqueous $Co(NO_3)_2 \cdot 6H_2O$ solution (1 mg mL^{-1}) and dispersed using sonication for 5 min. The solution was evaporated by heating in a water bath at 353 K, after which the powder was collected and heated at 773 K for 1 h under a flow of NH_3 (200 mL min^{-1}).

Characterization

XRD patterns of the prepared samples were recorded using a MiniFlex 300, Rigaku. using Cu-Kα radiation at 40 kV and 15 mA over a 2θ range of 10° to 60° with a step size of 0.017° and counting time of 80 s per step. SEM was performed with a JEOL JSM-7600F microscope and SEM-EDX mappings were acquired by employing a FESEM TESCAN S9000G. TEM and HRTEM images were obtained using an FEI Tecnai G2 F30 Spirit microscope operated at an accelerating voltage of 300 kV. UV-vis DRS (V-670, JASCO) was conducted over the range of 200–1000 nm using $BaSO_4$ as the reflectance standard. XPS was conducted using a Thermo Scientific ESCALAB 250Xi spectrometer and the decumulation of the peaks was carried out using the software of Avantage. EIS measurements were performed on an electrochemical analyser (CHI660C instruments) in a standard three-electrode system utilizing the synthesized samples as the working electrodes, Ag/AgCl (saturated KCl) as a reference electrode, and a Pt wire as the counter electrode. 0.2 M Na_2S and 0.04 M Na_2SO_3 mixed aqueous solution was used as the electrolyte.

Photocatalytic reactions

The photocatalytic reactions were performed in a top-irradiation-type reaction vessel with a Pyrex window using a Perfect 6A reaction system. For both H_2 and O_2 evolution, 0.3 g of the photocatalyst was dispersed in 150 mL of a 20 vol% aqueous methanol solution. Before photoirradiation, the reaction system was evacuated to remove all air and then irradiated from the top using a 300 W xenon lamp equipped with a dichroic mirror and a cut-off filter ($\lambda \geq 420$ nm). The reactant solution was maintained at 288 K using a cooling-water system during the reaction. The reaction was carried out for 5 h, and the gas production was analyzed every 30 min using an online analysis system with a gas chromatograph (GC-9790II) equipped with a thermal conductivity detector with N_2 as the carrier gas.

Conflicts of interest

There are no conflicts to declare.

Acknowledgements

Notes and references

1 Y. Qi, J. Zhang, Y. Kong, Y. Zhao, S. Chen, D. Li, W. Liu, Y. Chen, T. Xie, J. Cui, K. Domen and F. Zhang, *Nat. Commun.*, 2022, **13**, 484.

2 T. Takata, J. Jiang, Y. Sakata, M. Nakabayashi, N. Shibata, V. Nandal, K. Seki, T. Hisatomi and K. Domen, *Nature*, 2020, **581**, 411–414.

3 Y. H. Hong, Y.-M. Lee, W. Nam and S. Fukuzumi, *J. Am. Chem. Soc.*, 2022, **144**(2), 695–700.

4 K. Sivula and R. van de Krol, *Nat. Rev. Mater.*, 2016, **1**, 15010.

5 Y. Tachibana, l. Vayssieres and J. R. Durrant, *Nat. Photonics*, 2012, **6**, 511–518.

6 Q. Wang, M. Nakabayashi, T. Hisatomi, S. Sun, S. Akiyama, Z. Wang, Z. Pan, X. Xiao, T. Watanabe, T. Yamada, N. Shibata, T. Takata and K. Domen, *Nat. Mater.*, 2019, **18**, 827–832.

7 C. Pan, T. Takata, M. Nakabayashi, T. Matsumoto, N. Shibata, Y. Ikuhara and K. Domen, *Angew. Chem., Int. Ed.*, 2015, **54**, 2955–2959.

8 B. Tian, B. Tian, B. Smith, M. C. Scott, R. Hua, Q. Lei and Y. Tian, *Nat. Commun.*, 2018, **9**, 1397.

9 K. Maeda, Y. Tokunaga, K. Hibino, K. Fujii, H. Nakaki, T. Uchiyama, M. Eguchi, D. Lu, S. Ida, Y. Uchimoto and M. Yashima, *ACS Appl. Energy Mater.*, 2018, **1**, 1734–1741.

10 Y. Tang, K. Kato, T. Oshima, H. Mogi, A. Miyoshi, K. Fujii, K. Yanagisawa, K. Kimoto, A. Yamakata, M. Yashima and K. Maeda, *Inorg. Chem.*, 2020, **59**, 11122–11128.

11 B. Siritanaratkul, K. Maeda, T. Hisatomi and K. Domen, *ChemSusChem*, 2011, **4**, 74–78.

12 B. Siritanaratkul, K. Maeda, T. Hisatomi and K. Domen, *ChemSusChem*, 2011, **4**, 74–78.

13 M. Kodera, Y. Moriya, M. Katayama, T. Hisatomi, T. Minegishi and K. Domen, *Sci. Rep.*, 2018, **8**, 15849.

14 T. Hisatomi, C. Katayama, Y. Moriya, T. Minegishi, M. Katayama, H. Nishiyama, T. Yamada and K. Domen, *Energy Environ. Sci.*, 2013, **6**, 3595–3599.

15 X. Wang, T. Hisatomi, J. Liang, Z. Wang, Y. Xiang, Y. Zhao, X. Dai, T. Takata and K. Domen, *J. Mater. Chem. A*, 2020, **8**, 11743–11751.

16 S. Ida, Y. Okamoto, M. Matsuka, H. Hagiwara and T. Ishihara, *J. Am. Chem. Soc.*, 2012, **134**, 15773–15782.

17 K. Maeda, Y. Tokunaga, K. Hibino, K. Fujii, H. Nakaki, T. Uchiyama, M. Eguchi, D. Lu, S. Ida, Y. Uchimoto and M. Yashima, *ACS Appl. Energy Mater.*, 2018, **1**, 1734–1741.

18 J. Seo, T. Hisatomi, M. Nakabayashi, N. Shibata, T. Minegishi, M. Katayama and K. Domen, *Adv. Energy Mater.*, 2018, **8**, 1800094.

19 T. Hryniewicz, K. Rokosz and H. R. Z. Sandim, *Appl. Surf. Sci.*, 2012, **263**, 357–361.

20 Y.-I. Kim, P. M. Woodward, K. Z. Baba-Kishi and C. W. Tai, *Chem. Mater.*, 2004, **16**, 1267–1276.

21 Y. Tang, K. Kato, T. Oshima, H. Mogi, A. Miyoshi, K. Fujii, K. Yanagisawa, K. Kimoto, A. Yamakata, M. Yashima and K. Maeda, *Inorg. Chem.*, 2020, **59**, 11122–11128.

22 K. Momma and F. Izumi, *J. Appl. Crystallogr.*, 2011, **44**, 1272.

23 I. P. Roof, T.-C. Jagau, W. G. Zeier, M. D. Smith and H.-C. Loye, *Chem. Mater.*, 2009, **21**, 1955–1961.

24 J.-H. Liao and M.-C. Tsai, *Cryst. Growth Des.*, 2002, **2**, 83–85.

25 L. Wan, F.-Q. Xiong, B. Zhang, R. Che, Y. Li and M. Yang, *J. Energy Chem.*, 2018, **27**, 367–371.

26 Y. Du, L. Yuan, K. Huang and S. Feng, *J. Lumin.*, 2013, **135**, 196–200.

27 K. Korzeniowski and M. Sobczyk, *Solid State Commun.*, 2018, **273**, 30–33.

28 V. R. Reddy, D. W. Hwang and J. S. Lee, *Catal. Lett.*, 2003, **90**, 39–43.

29 M. Hojamberdiev, E. Zahedi, E. Nurlaela, K. Kawashima, K. Yubuta, M. Nakayama, H. Wagata, T. Minegishi, K. Domen and K. Teshima, *J. Mater. Chem. A*, 2016, **4**, 12807–12817.

30 X. Wang, T. Hisatomi, Z. Wang, J. Song, J. Qu, T. Takata and K. Domen, *Angew. Chem., Int. Ed.*, 2019, **58**, 10666–10670.

31 J. Seo, S. Jeong and S. Kim, *ACS Appl. Energy Mater.*, 2021, **4**, 3141–3150.

32 V. Khanal, N. O. Balayeva, C. Günnemann, Z. Mamiyev, R. Dillert, D. W. Bahnemann and V. (Ravi) Subramanian, *Appl. Catal., B*, 2021, **291**, 119974.

33 Y. Okamoto, S. Ida, J. Hyodo, H. Hagiwara and T. Ishihara, *J. Am. Chem. Soc.*, 2011, **133**, 18034.

34 H. Zhang, S. Wei and X. Xu, *J. Catal.*, 2020, **383**, 135–143.

35 G. R. Dillip, A. N. Banerjee, V. C. Anitha, B. D. P. Raju, S. W. Joo and B. K. Min, *ACS Appl. Mater. Interfaces*, 2016, **8**, 5025–5039.

36 S. Chen, S. Shen, G. Liu, Y. Qi, F. Zhang and C. Li, *Angew. Chem., Int. Ed.*, 2015, **54**, 3047–3051.

37 B. Dong, J. Cui, T. Liu, Y. Gao, Y. Qi, D. Li, F. Xiong, F. Zhang and C. Li, *Adv. Energy Mater.*, 2018, **8**, 1801660.

38 C. Peng, T. Zhou, P. Wei, H. Ai, B. Zhou, H. Pan, W. Xu, J. Jia, K. Zhang, H. Wang and H. Yu, *Chem. Eng. J.*, 2022, **439**, 135685.